Electrochimica Acta 443 (2023) 141930

Contents lists available at ScienceDirect

Electrochimica Acta

journal homepage: www.journals.elsevier.com/electrochimica-acta

A comparative study of different sol-gel coatings for sealing the plasma electrolytic oxidation (PEO) layer on AA2024 alloy

Sajjad Akbarzadeh [a,b,*], Yoann Paint [c], Marie-Georges Olivier [a,c]

[a] Materials Science Department, Faculty of Engineering, University of Mons, 20, Place du Parc, Mons, Belgium
[b] Metallurgy Department, Faculty of Engineering, University of Mons, 20, Place du Parc, Mons, Belgium
[c] Materia Nova Research Centre, 1, Avenue N. Copernic, Parc Initialis, Mons, Belgium

ARTICLE INFO

Keywords:
Sol-gel precursors
Plasma electrolytic oxidation
Sealing
EIS
SVET

ABSTRACT

Owing to the inherent porosity of the coatings produced through the PEO process, the application of sol-gel coatings as a post-treatment has drawn immense attention thanks to their eco-friendly and reliable protective characteristics. Various parameters affect their performance, and the type of sol-gel precursors plays a significant role. In this study, various sol-gel precursors were used to prepare four types of PEO/sol-gel coating systems followed by an investigation of their sealing ability and corrosion resistance properties on AA2024 alloy. The corrosion prevention performance of the coatings was studied by electrochemical impedance spectroscopy (EIS) along with Scanning Vibrating Electrode Technique (SVET) analyzes. Some chemical characterization tests, such as Fourier Transform Infrared Spectroscopy (FT-IR) and rheology measurement, affirmed the influence of the sol-gel chemical composition on its compactness and the network viscosity. The distinctive sealing ability of different sol-gel coatings for the defects and pore filling of the PEO layer was visualized by Scanning Electron Microscope (SEM). To this end, different sol-gel formulations and various sol-gel network properties accordingly caused dissimilar sealing features for the PEO pores and, subsequently, the corrosion resistance of the duplex PEO/sol-gel coating is widely dependent on the used sol-gel precursors.

1. Introduction

The reliable weight-to-strength ratio of aluminum alloys, especially the Al-Cu-Mg system (2xxx series), makes them extensively applicable in automotive and aerospace fields [1]. Major elements, denoted as Al_6(Cu, Mn, Fe), plus S-phase intermetallic particles (IMPs), represented as Al_2CuMg, are two copper sources in AA2024 alloy. Despite acceptable mechanical characteristics, the vulnerability of AA2024 to localized corrosion is a major drawback [2,3]. Its low resistance to a local type of corrosion owing to the poor protective properties of the passive layer on the S-phase in any case of probable fluctuation or heterogeneity exposes the bare metal to aggressive electrolytes [4]. To compensate for its deficiency, a surface treatment is strongly recommended [5]. During recent decades, various surface modifications, such as conversion coatings [6], chemical vapor deposition (CVD) [7], physical vapor deposition (PVD) [8], thermal spraying [9], diffusion treatment [10], ion implantation [11], anodization [12], and PEO, have been employed to enhance the corrosion resistance properties of aluminum alloys [13]. Among these techniques, PEO plays a crucial role thanks to its eco-friendly properties along with producing dense, hard, and thick ceramic coatings on light alloys [14]. In particular, PEO coatings have been more auspicious than hard-chrome plating and hard anodizing for applications requiring high wear resistance [15].

PEO, as a cost-effective and efficient surface treatment, has been employed for various light alloys, such as Ti, Mg, and Al, to attain a protective oxide layer [16–20]. This technique, in comparison to anodizing, is applied at a higher voltage associated with electrochemical reactions, plasma reactions, and species diffusion at the working electrode. A diluted alkaline water-based electrolyte is generally utilized for the PEO process which can be considered more environment-friendly than anodizing technology [21,22]. During the PEO process, uncountable ephemeral micro-arcs appear on the surface which dramatically increase the temperature and pressure in local sites. Once micro discharges take place over the surface, the oxide layer is intended to melt and solidify frequently, provoking the incorporation of the oxide layer with the electrolyte components as well as promoting the creation of high-temperature phases [23,24]. Consequently, a ceramic coating with improved corrosion resistance, hardness, and wear properties are

---

[*] Corresponding author at: Materials Science Department, Faculty of Engineering, University of Mons, 20, Place du Parc, Mons, Belgium.
E-mail address: marjorie.olivier@umons.ac.be (M.-G. Olivier).

https://doi.org/10.1016/j.electacta.2023.141930
Received 1 November 2022; Received in revised form 20 December 2022; Accepted 21 January 2023

obtained. Specifically, the PEO layer on the aluminum alloy is comprised of internal and porous sublayers in which the presence of the latter is a drawback for long-term corrosion resistance [25,26].

The inherent pores of a PEO layer can be sealed by precipitation of low-soluble products in some post-treatments, like hydrothermal treatments and conversion coatings [27–30]. Among various surface post-treatments, the application of a sol-gel coating has become a promising method thanks to its eco-friendly properties, ease of fabrication, and process flexibility [31–34]. Several factors affect sol-gel characteristics, such as solution pH, aging, type of solvent, and particularly the type of sol-gel precursor which plays a leading role in its performance [35,36]. The sol-gel process can be defined as the formation of an oxide network in a liquid by continuous condensation reactions of a precursor [37]. Mainly, it commences with a low molecular weight organic solution, like alcoholic ones containing metal or metalloid alkoxide precursors denoted as $M(OR)_n$, where M is the network-forming element (Al, Zr, Ti, Si, etc.) and R represents an alkyl ligand (C_nH_{2n+1}). Hybrid materials are typically produced by the sol-gel process. Silicon or non-silicon alkoxide is most commonly the inorganic phase, whereas hydrolysis and condensation reactions are in charge of the modification of the organic phase of silicon alkoxide [38]. Speaking of the combination of various metal alkoxides, the metal alkoxide activity and the type of the catalyst are considered determining factors of the morphology and structure of the network evolution. To restrain the hydrolysis and condensation reactions of non-silicon metal alkoxide chelating ligands, for instance, organic acids are used [39,40]. Regarding this, the combination of zirconium tetrapropoxide (ZTP) and methacrylic acid (MAA) is proven in terms of stability and corrosion resistance properties [41].

Merino et al. revealed the improvement impact of sol-gel sealing based on Tetraethyl orthosilicate (TEOS) and (3-Glycidyloxypropyl) trimethoxysilane (GPTMS) precursors for the PEO layer on AZ31B Mg alloy [42]. Pezzato et al. corroborated the sealing performance of the mixture of TEOS and Methyltriethoxysilane (MTES) for PEO layers produced on AZ80 magnesium alloy and 7020 aluminum alloy [43]. Toorani et al. examined the best consumption ratio of TEOS and (3-Aminopropyl)triethoxysilane (APTES) to seal the porous layer of PEO on AZ31B Mg alloy [44]. The significant corrosion prevention improvement of a PEO layer on a secondary cast Al-Si alloy was obtained elsewhere by employing TEOS along with MTMS precursors [45].

In this study, different combinations of sol-gel precursors (Fig. 1), including TEOS, MTES, GPTMS, APTES, ZTP, and 3-(trimethoxysilyl) propyl methacrylate (MAPTMS), were employed to prepare four distinct sol-gel solutions. The existence of four hydrolyzable groups in the chemical structure of TEOS is the reason for being in all four types of sol-gel solutions as the key network-forming component. Then, the sealing ability and corrosion resistance properties of the duplex PEO/sol-gel coating system on AA2024 alloy were scrutinized. The electrochemical response of the coating samples was acquired by the EIS measurements as well as SVET mapping in the simulated aggressive solutions. The hydrophobicity characteristics of the duplex coating system were studied by water contact angle (WCA) along with plenty of chemical characterization analyzes, such as FT-IR and flow curves obtained using a rheometer.

2. Experiment and methods

2.1. Materials preparation

2.1.1. Substrate preparation

AA2024 alloy with the dimensions of 3 cm × 3 cm × 0.16 cm and the chemical composition summarized in Table 1 was employed as the substrate. Prior to the PEO procedure, the alloy panels were cleaned via ultrasonication in acetone for 10 min. The coupons underwent alkaline etching (NaOH) for 30 s at 40 ℃ followed by acid pickling in HNO_3 solution at room temperature for 30 s.

2.1.2. PEO coating

The PEO process was carried out by utilizing a bipolar power supply (Micronics Systems, France) using a squared pulsed regime with 5 A of anodic current and 100 Hz for half an hour [46,47]. The *RCQ* parameter [48] which defines the ratio of positive (Q_p) to negative (Q_n) charge quantities applied during one period of the current pulse was 0.9 in this investigation. The duty cycle (D_t) which is described in the below

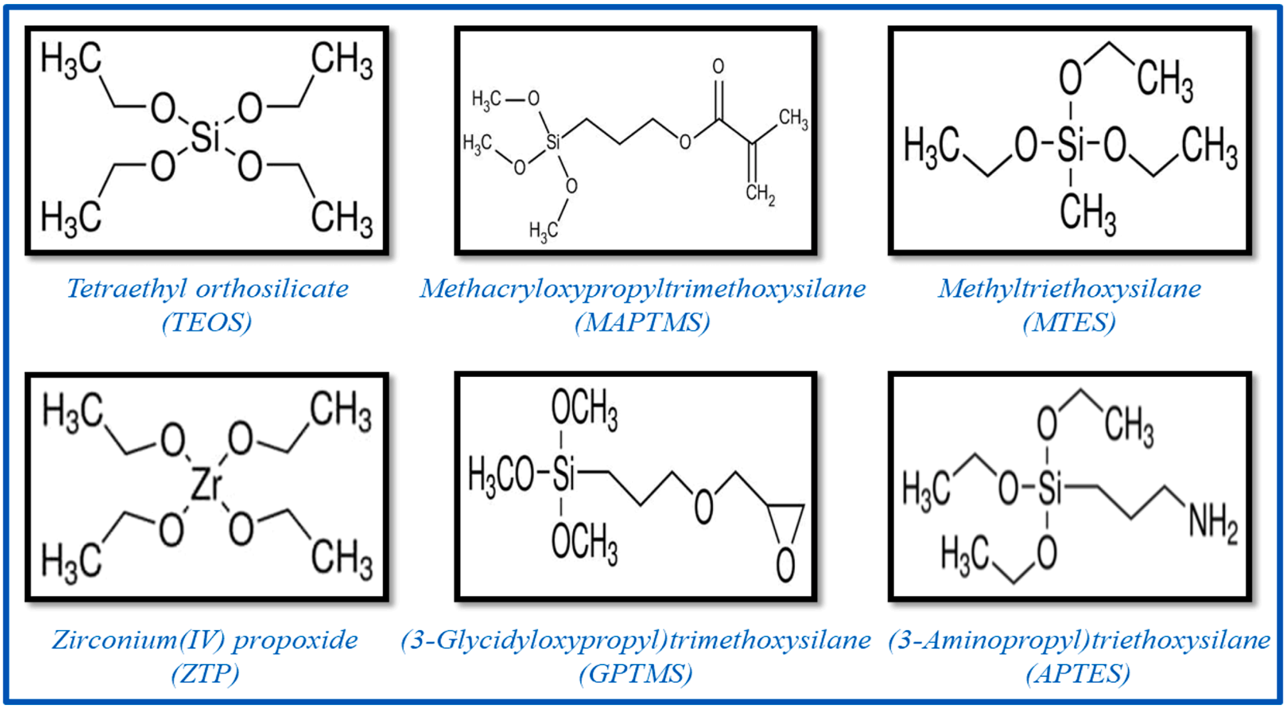

Tetraethyl orthosilicate (TEOS)

Methacryloxypropyltrimethoxysilane (MAPTMS)

Methyltriethoxysilane (MTES)

Zirconium(IV) propoxide (ZTP)

(3-Glycidyloxypropyl)trimethoxysilane (GPTMS)

(3-Aminopropyl)triethoxysilane (APTES)

Fig. 1. The molecular structure of various sol-gel precursors to obtain different types of sol-gel coatings.

Table 1
The nominal composition of the AA2024 substrate panels.

Element	Ti	Ni	Zn	Si	Fe	Mn	Mg	Cu	Al
%wt.	≤0.15	≤0.15	≤0.25	≤0.5	≤0.5	0.3–0.9	1.2–1.8	3.8–4.9	Balance

equation was set at 30%:

$$D_t = \left[t_{on} / \left(t_{on} + t_{off}\right)\right] \times 100 \quad (1)$$

where t_{on} is the 'on' duration and t_{off} is the 'off' duration during a single cycle [49].

The electrolyte was in a double-walled container consisting of Na_2SiO_3 and KOH (Alfa Aesar Co.) with a concentration of 1.65 g/l and 1 g/l, respectively. The electrolyte cell was coupled with a cooling apparatus to keep the temperature below 40 °C during the PEO process.

2.1.3. *Sol-gel formulations*

Four types of sol-gel solutions were obtained by different combinations of the sol-gel precursors. The first sol-gel solution, denoted as SG, comprised TEOS (20% V/V) and GPTMS (10% V/V) in an electrolyte consisting of distilled water (60% V/V) and ethanol (10% V/V). Acetic acid was utilized to adjust the pH to 3 then the solution was mixed for 24 h [50]. Another sol-gel solution (SG-MT) consisted of an equally volumetric intake of three precursors, including TEOS (10% V/V), GPTMS (10% V/V), and MTES (10% V/V). In other words, for the formulation of the SG-MT, the amount of TEOS in the SG solution decreased to 10% V/V, and instead, the MTES precursor with the concentration of 10% V/V was added to obtain the SG-MT sol-gel solution. As for the SG formulation, the same composition of the water-based electrolyte with a pH of 3 was employed and was subsequently mixed for 24 h to complete sol-gel network reactions before the coating application. The PEO-coated samples with these two solutions were placed in the oven at 150 °C for 1 h. For another sol-gel solution (SG-AP), a similar volumetric intake of APTES (15% V/V) and TEOS (15% V/V) was utilized to get the overall percentage of 30% V/V silane precursors in a solution containing ethanol (56% V/V) and distilled water (14% V/V). Afterwards, the pH of the solution was kept at 4.5 by adding acetic acid drop-by-drop to the solution. The solution was mixed for one day at ambient temperature to get a transparent solution confirming the complete hydrolysis reactions [51]. The PEO sample coated with SG-AP solution was placed at ambient temperature for 24 h followed by putting it in an oven at 150 °C for 1 h. Finally, the sol-gel formulation is based on the optimization work of Peter Rodič et al. [52] and is denoted as SG-ZT in which two types of sol-gel solutions were employed. The first solution (sol 1) was composed of TEOS (0.18 mol) and MAPTMS (1 mol) precursors whose hydrolysis and condensation reactions were initiated by the dropwise addition of distilled water (2.075 mol) and hydrochloric acid (0.001 mol). Then after 150 min stirring, it was added dropwise to sol 2 which had been stirred for half an hour, then the product was mixed for one day to ensure the development of hydrolysis and condensation reactions. Sol 2 contained ZTP (0.12 mol), MAA (0.12 mol), and isopropyl alcohol (0.4 mol). Drying of the coated samples with SG-ZT solution was conducted for 1 h at 100 °C. All PEO specimens were coated via a KSV Nima dip-coater instrument at a 100 mm/min withdrawal rate. Sol-gel precursors, organic acids, and solvents were purchased from VWR. The PEO samples coated with SG, SG-MT, SG-AP, and SG-ZT were denoted as PSG, PSG-MT, PSG-AP, and PSG-ZT, respectively.

2.2. *Methods and techniques*

2.2.1. *Characterization tests*

The flow curves and viscosity determination of the different sol-gel solutions were reported via the Anton Paar apparatus. The rheology measurements were carried out in the DG-41 cylinder at a constant temperature of 26 °C in which shear rates varied from 0 to 200 s^{-1}. Fine dried droplets of sol-gel solution were obtained to conduct the FT-IR test with IRTracer-100 (Shimadzu Co.) within the 600–4000 cm^{-1} wavenumber range. The cross-section visualization and surface morphology of the PEO layer coated with various types of sol-gel solutions were reflected by the SEM technique, using Hitachi SU8020 equipment along with energy dispersive X-ray spectroscopy (EDS). The EDS facility was equipped with a Thermoscientific Noran System 7 detector to provide a bright insight into the chemical composition of the samples. The hydrophobic properties of different panels were examined through the water contact angle (WCA) test, employing the DSA10-MK2 KRUSS instrument. Five examinations were performed for each case to ascertain the reproducibility of the outcome.

2.2.2. *Electrochemical investigations*

The corrosion-resistance properties of the coupons were examined by EIS with the BioLogic SP-300 apparatus in 0.1 M NaCl solution. The typical three-electrode set-up was utilized whose auxiliary, reference, and working electrodes were platinum electrode, Ag/AgCl/KCl (+197 mV/SHE) electrode, and coated panel, respectively. The EIS outcomes were gathered from 100 kHz to 100 mHz frequency, employing a sine wave oscillation with ±10 mV peak-to-peak amplitude. The exposed area of the coupons to the aggressive solution was 1.0 cm^2 and for each group of samples, at least two measurements were carried out at any immersion times to investigate their reproducibility. To this end, the EIS findings were curve-fitted by the most appropriate electrical equivalent circuit (EEC) in the framework of ZView software to attain all electrochemical parameters playing a role in the corrosion phenomenon.

SVET (Applicable Electronics (AE)) was conducted from the cut-edge configuration of the coated samples that were embedded in epoxy resin (EpoFix) followed by abrasion with sandpapers to 2400 grit size. The cross-section was covered by 3 M™ Scotchrap™ 50 tape with 1 mm^2 unmasked to expose to 15 mM NaCl (604 Ωcm) solution. The tip of the SVET probe (platinum/iridium) was platinized based on the equipment instruction manual to enhance its capacitance thanks to an increase in surface area. The probe distance from the sample surface, the probe diameter, and the vibration amplitude were 200 µm, 20 µm, and 40 µm, respectively. The cut-edge exposed area was scanned with a 21 × 21 grid point and the test was done twice for each sample to assert its reproducibility. The schematic illustration of the cut-edge setup is exhibited in Fig. 2.

3. Results and discussion

3.1. *FT-IR spectroscopy*

In order to gain a better insight into the chemical structure of the sol-gel coatings, the FT-IR test was carried out and the outcome is presented in Fig. 3. It is widely accepted that silica cluster formation initiates by the hydrolysis of ethoxy groups, leading to the creation of silanol groups. Meanwhile, condensation reactions take place to form chains and grow the particles [53,54]. By a glance at the spectra, the intense peak at around 1020 cm^{-1}, which is related to the Si-O-Si band, confirms the silica network formation by hydrolysis and condensation reactions in all types of coatings [55]. Whereas the presence of C-H stretching peaks at 2870 cm^{-1} and 2922 cm^{-1} were respectively related to the unreacted ethoxide and methoxide groups [56,57]. Considering the lower number of hydrolyzable groups in the structure of MTES than TEOS, the addition of MTES to the SG-MT formulation resulted in the presence of a Si-C peak at 1280 cm^{-1} due to the presence of the methyl non-hydrolyzable group in the MTES precursor [58]. It is worthwhile to mention that due to the

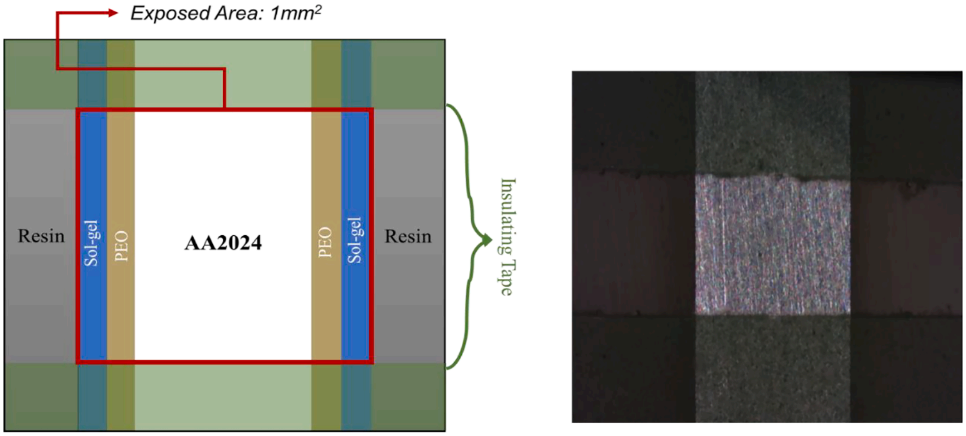

(a) (b)

Fig. 2. The cut-edge configuration for the SVET analysis in the schematic (a) and experimental (b) representations.

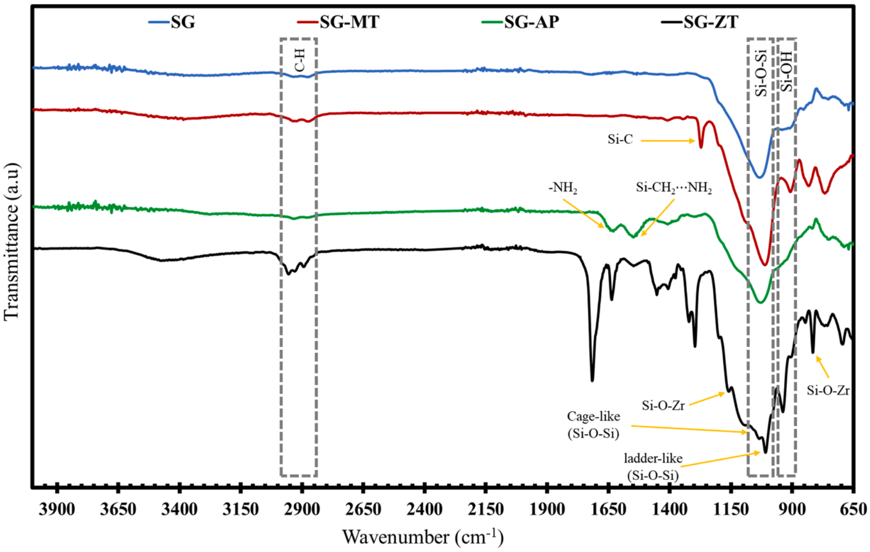

Fig. 3. The FT-IR results of different sol-gel formulations.

same coating conditions for SG and SG-MT, the network density of the SG-MT might be lower than SG based on the presence of one non-hydrolyzable group in the structural body of the MTES molecule. In the SG-AP sample, the amine groups in the APTES, and the Si-CH_2 linked to the -NH_2 groups, are likely attributed to the peaks at 1629 cm^{-1} and 1535 cm^{-1}, respectively [59,60]. Since two different sols were added for the preparation of SG-ZT, the polycondensation of residual metal alkoxyl groups and hydroxyl groups would be expected, leading to the formation of a three-dimensional group [61]. As can be seen in the domain of 1020 cm^{-1} to 1200 cm^{-1} some additional peaks appeared compared to the other sol-gel samples. To enumerate, the peak at 1020 cm^{-1} with the shoulder at 1075 cm^{-1} reflected the ladder-like and cage-like structures of the Si-O-Si network [62]. It has been reported that cage-like oligosiloxanes are reputed as molecular building blocks, forming a denser network matrix [63–65]. Consequently, the relatively higher barrier performance of the SG-ZT coating against penetration of the aggressive elements could be anticipated. It is noteworthy to mention that hetero-condensation (Si-O-Zr) occurs along with homo-condensation (Si-O-Si) confirmed by peaks at 814 and 1138 cm^{-1}. The peaks at 1404 and 1452 cm^{-1} are related to the C-H vibration bond, originating from the presence of MAA, MAPTMS, and aliphatic C-H groups in the propoxide. Additionally, the presence of MAA and MAPTMS can be corroborated by peaks at 1635, 1705, and 1721 cm^{-1} [66,67].

3.2. Rheology test

The viscosity versus shear rate measurement demonstrated the Newtonian response of the different sol-gel solutions (Fig. 4). The presence of a reactive amino group in the APTES molecule and its inherent inclination to take part in competition reactions resulted in a higher viscosity of SG-AP (3.7 ± 0.2 mPa.s) than SG (3.5 ± 0.2 mPa.s) [68,69]. The amino group in APTES can react with the silanol group during hydrolysis and condensation reactions via hydrogen bonding or electrostatic attractions, whereas the epoxy functional end-group in the GPTMS remains stable upon network formation. Although, it is believed that epoxy ring opening occurs at elevated temperatures during curing [70]. The methyl-silicon bond of MTES is unreacted upon matrix evolution in SG-MT, which is why the addition of MTES to the sol-gel formulation (less intake of TEOS precursor) brings about the decrement of network density and subsequently its viscosity. Therefore, the viscosity of SG-MT (3.2 ± 0.1 mPa.s) is less than SG. On the other hand, the relatively high content of sol-gel precursors in the SG-ZT compared to the others makes it the most viscous sol-gel among them (11.5 ± 0.3 mPa.s). Moreover, by mixing two sol-gel solutions during the preparation of SG-ZT, the polycondensation of metal alkoxy groups and the

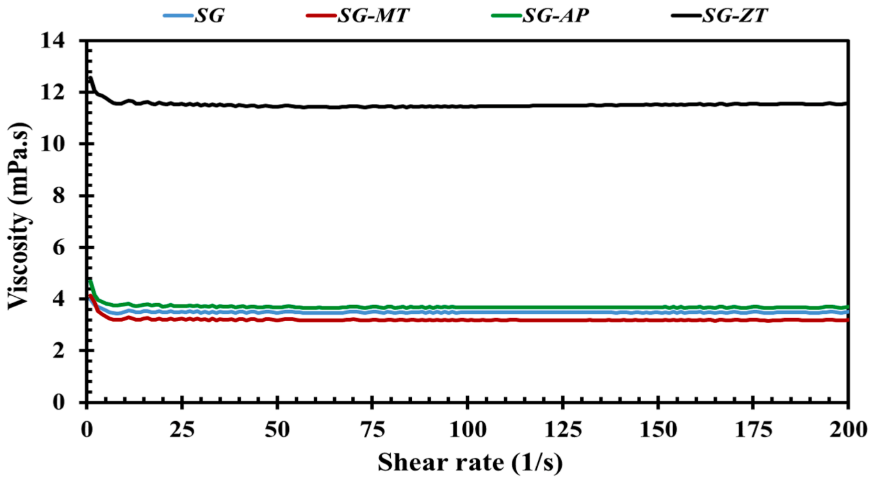

Fig. 4. Flow curves of various types of sol-gel solutions.

residual hydroxyl group takes place, leading to the intensification of the SG-ZT viscosity. As a side note, the higher the solution viscosity, the thicker the film on a substrate [71]. But in terms of corrosion resistance properties of a PEO layer, some crucial factors, such as the sealing ability of the inherent pores, network compactness, wettability characteristics, etc., play significant roles.

3.3. *SEM observation*

3.3.1. *Top-view images*

The surface morphology of the coated samples was examined through SEM images illustrated in Fig. 5. The repetitive melting/solidifying of the oxide layer during the PEO process in the silicate-containing solution generates typical porous features on aluminum

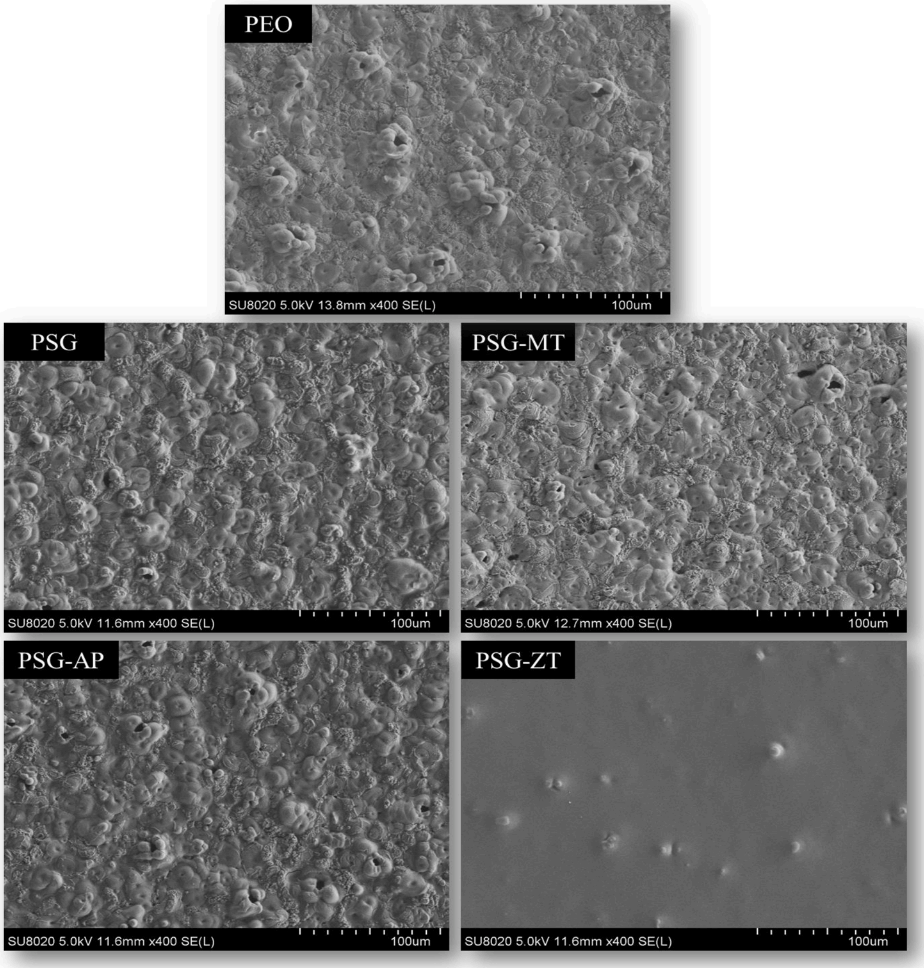

Fig. 5. Surface topography of the PEO layer after application of different types of sol-gel coatings.

alloys. The dielectric breakdown, followed by plasma reactions and the creation of some sparks, could produce unnumbered pores distributed randomly over the surface with a diameter ranging from 1 to 10 μm. By application of SG and SG-MT, most of the pores were filled, even though some relatively huge ones were still observed. Although the presence of the SG-AP coating could be sensed on the PEO layer, it could not completely fill the pores as the number of open-mouth pores was almost unchanged as compared to the PEO sample. While in the PSG-ZT sample, the fabrication of the homogenous sol-gel layer on the PEO layer is observed which covered the porous layer, and the PEO layer was no more detectable except for a few pore initiations.

3.3.2. Cross-section images

The cross-section observation coupled with EDS mapping of the PEO plus various sol-gel applications are presented in Fig. 6. The presence of Si, O, and Al has come from the fact that the PEO oxide layer, with a thickness of 14.92 ± 4.9 μm, was produced by the combination of the silicate solution and substrate elements. Furthermore, the Si element can be considered as the element for the presence of all types of sol-gel coatings, plus Zr for the PSG-ZT specifically. There was no big difference that could be distinguished between PSG and PSG-MT in terms of sealing ability as both sol-gels could penetrate through pores, microcracks, and channels. In these two cases, the Si element in the mapping images was intensified, reflecting the presence of the sol-gel coating either inside the porous layer or on the PEO layer. Being a GPTMS precursor in the formulation of the SG and SG-MT sol-gels facilitates the pore-filling possibility [72,73]. The presence of some pores in the PSG-AP sample revealed that the SG-AP could not penetrate and seal the PEO pores in the desired way. In this case, SG-AP is mainly located at the top surface of the PEO layer as indicated by a higher Si content at this compared to the PSG and PSG-MT layer. In other words, the SG-AP seemed to not be inclined to penetrate through the pores and precipitates over the PEO surface. Thus, as highlighted in the SEM and EDS cross-section, there is an unsealed pore on the right-hand side of the PSG-AP, demonstrating that the SG-AP predominantly emerged on the surface as opposed to diffusing into the pores and cracks. In parallel to the top-view images, the production of the homogeneous top sol-gel layer with a thickness of 8.62 ± 2.42 μm could be observed in the PSG-ZT sample. Interestingly, the SG-ZT not only created the layer on the PEO coating but also diffused through the channels and pores and sealed any kinds of deficiencies despite its higher viscosity. The presence of Zr along with Si element in the EDS mapping also confirmed the creation of the sol-gel network in the SG-ZT by two network elements.

3.4. WCA examination

The wettability of the coated samples on the PEO layer was examined through the WCA test and illustrated in Fig. 7. All types of sol-gel coatings increased the hydrophobicity of the PEO layer in which the WCA reached almost 88° (PSG-ZT) from 27°. Upon sol-gel network formation, hydrolysis reactions happen which turn alkoxy groups into hydrophilic silanol groups. Then the hydrolyzed molecules are attracted either to deposit on a metal surface (Si-O-M) or to form a siloxane (Si-O-Si) network which is more hydrophobic than silanol groups [74]. The hydrophobic feature of the SG-MT is higher than SG owing to the presence of non-polar methyl terminated groups in the MTES precursor [75,76]. Interestingly PSG-AP had the lowest hydrophobicity among the other samples which is in parallel with another study. In fact, it originates from the fact that the PSG-AP film has unnumbered amino groups (-NH_2) having an outward orientation from the metal surface [77]. These amino end-groups can be considered as appropriate reactive sites to form hydrogen bonds with water molecules and, consequently, the hydrophilic properties of the surface are enhanced. On the other hand, the polycondensation reactions of residual hydroxyl and metal alkoxy groups, which arise from the mixing of the two sols during the preparation of SG-ZT along with homogenous surface morphology, made the PSG-ZT sample the most hydrophobic coating system. Furthermore, the presence of significant organic parts being hydrophobic in nature in the

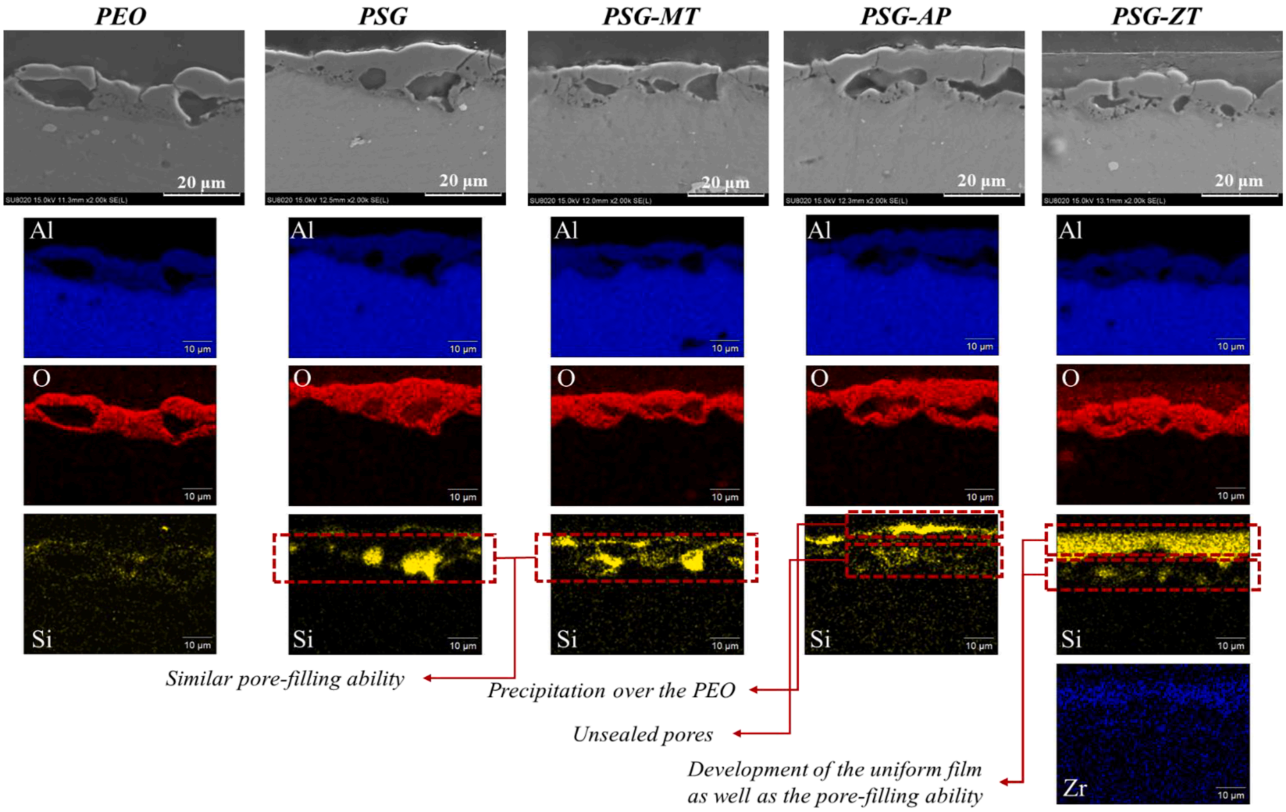

Fig. 6. SEM images from cross-section along with EDS mapping illustrations of different types of PEO/sol-gel duplex coating systems.

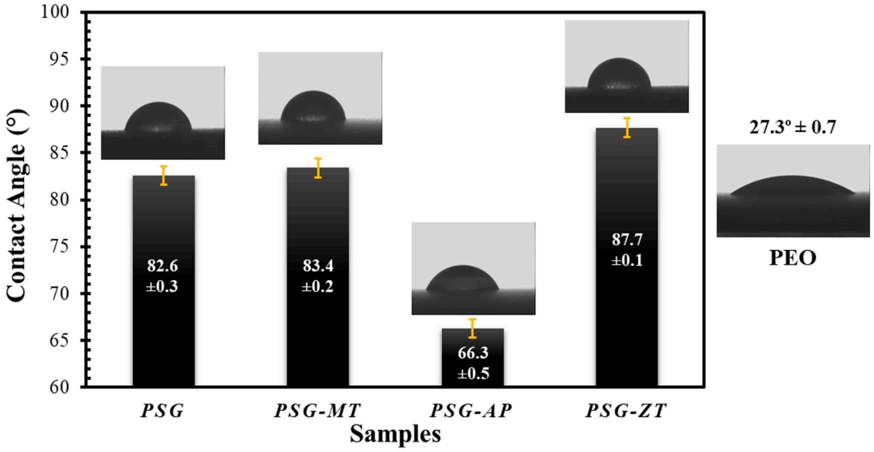

Fig. 7. The WCA inspection of the PEO sample along with PEO/sol-gel duplex coating systems.

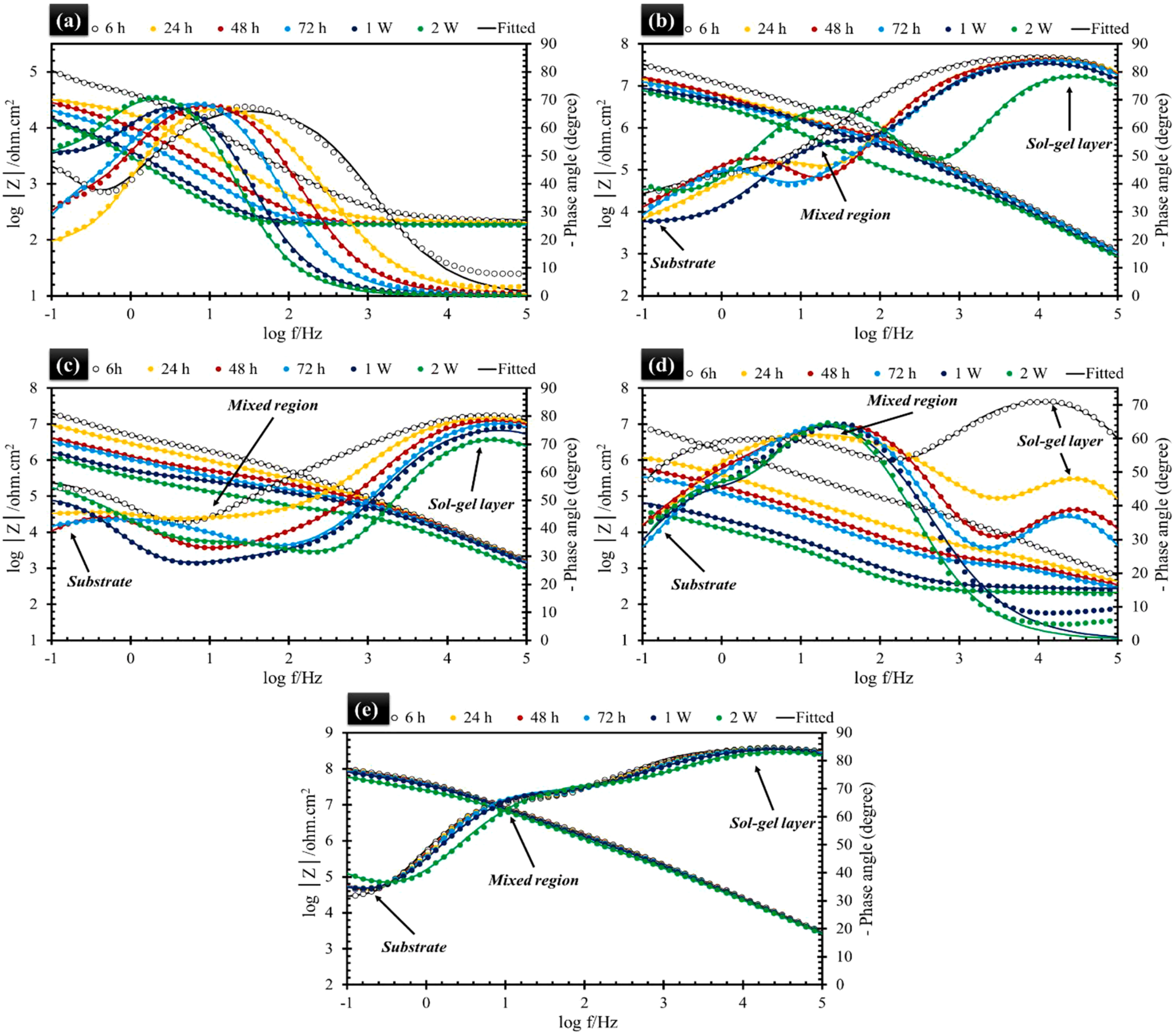

Fig. 8. Bode diagrams of PEO (a) plus various kinds of duplex PEO/sol-gel coatings corresponding to PSG (b), PSG-MT (c), PSG-AP (d), and PSG-ZT (e) after two weeks exposure to 0.1 M NaCl solution.

SG-ZT sol-gel composition, which is by far more than other sol-gel formulations, engendered the development of hydrophobic properties.

3.5. EIS results

The corrosion resistance of various sealing sol-gels on the PEO layer was evaluated by EIS test up to two weeks of immersion in the 0.1 M NaCl solution. The Bode diagrams of the samples are depicted in Fig. 8, respectively. Moreover, the EIS outcomes were fitted by several equivalent electrical circuits (EEC), demonstrated in Fig. 9, and the subsequently extracted electrochemical parameters are summarized in Table 2. Where R_e, R_{SG}, R_p, and R_{ct} are ascribed to the resistance of the electrolyte, sol-gel coating, PEO layer, and charge transfer, respectively. The fitting and experimental data are exhibited in the form of solid lines and markers in the EIS spectra, respectively. Roughness and heterogeneity make any surface a non-ideal interface, which is why the constant phase element (CPE) was considered in place of an ideal capacitor to elucidate the EIS results. The CPE impedance is determined through the below formula [78]:

$$Z_{CPE} = \left[\frac{1}{Y_0(\mathrm{i}\omega)^n}\right] \tag{2}$$

where n is the frequency dispersion factor varying from 0 (pure resistance) to 1 (pure capacitance) and the admittance of CPE is Y_0. The CPE element of the sol-gel, PEO, and double-layer is denoted as CPE_{SG}, CPE_p, and CPE_{dl}, respectively. Fabrication of sol-gel layers on the PEO porous layer resulted in the presence of a mixed region in which the sol-gel layer presented in a form of a cement-like material throughout the pores. Hence, the sealed porous region in the PEO coatings with a sol-gel layer is represented in terms of CPE_{mix} and R_{mix}.

The PEO process is generally characterized by two distinctive layers: an outer (porous) layer and an inner layer (thin) [79]. The presence of the porous layer is considered a deficiency for long-term protection as it generates diffusion pathways for the aggressive electrolyte to access the substrate. Based on the type of the EEC (Fig. 9a), two time-constants for the unsealed PEO sample refer to the inner thin layer and porous outer layer after 6 h immersion (the labels R_p and R_{ct} at 6 h of immersion for the PEO sample in Table 2 are actually the resistance of outer and inner layers, respectively). The fitting outcome reflected the higher resistance value for the inner layer as compared to the porous region, revealing that the short-term protection of the PEO layer primarily stems from the dense inner layer [80]. After 24 h, the coating starts to deteriorate, which is why the time constants were changed to include the entire coating (porous and inner) plus the substrate response. In fact, certain pores in the PEO layer either formed or extended, creating channels for the aggressive electrolyte to diffuse [81]. The employed EEC was changed from Fig. 9a to b as a result. The EEC in Fig. 9b, which represents a typical circuit for oxide layers, showed that R_p and CPE_p represent the PEO layer, while CPE_{dl} and R_{ct} refer to the substrate response [82]. Meaning that the decrement of the corrosion inhibition of the PEO after 24 h resulted in the development of certain pores deep enough to reach the substrate. Consequently, the circuit in Fig. 9b demonstrated that the sequence of permeation was divided into two levels by using a series circuit with two-time constants [83]. Moreover, it is also mentioned elsewhere that this EEC usually describes the homogeneous electrolyte diffusion into coatings causing uniformly distributed reaction sites at the interface [84]. The PEO sample thereafter exhibits this electrochemical activity for the duration of the immersion time (2 weeks). After the application of sol-gel coatings on the PEO layer, a new time constant appeared that can be noticed at high frequencies. Obviously, its broadening decreased by the elapsing immersion time owing to the propagation of corrosion reactions. The enlargement of the low-frequency impedance in Bode spectra confirmed the improvement of the corrosion protection properties of the distinct PEO layer after the fabrication of each sol-gel layer. However, the chemistry of different sol-gel layers could dramatically affect their anti-corrosion performance in longer immersion times.

For the PSG, the pores of the PEO layer were filled before the curing step by the combination of the TEOS and GPTMS precursors, which is why the three-time constant EEC in Fig. 9c was utilized. In the employed EEC, the existence of the sol-gel layer was confirmed at high frequencies, at the same time as the middle-range frequency response was attributed to the presence of the mixture of sol-gel and PEO layers. Apart from the fact of R_{SG} coming into existence, by comparing R_p and R_{mix} values in the PSG case, the pore filling of the SG for the porous PEO layer was also validated. Nevertheless, the lowering trend of R_{SG}, and accordingly the increasing tendency of the admittance component of CPE_{SG}, reports the deterioration of the SG barrier properties during exposure to the aggressive electrolyte.

The sealing ability of the PSG and PSG-MT is practically comparable, as seen by SEM cross-section pictures, which is why the same EEC (Fig. 9c) was used in all immersion times to extract the electrochemical data. In parallel to the FT-IR and rheology tests, the addition of the MTES to the formulation could decrease the cross-linking density owing to the presence of one nonhydrolyzable methyl group, therefore the compactness of SG-MT was less than SG. Although their sealing behavior was identical its compactness could affect the barrier protective performance. Regarding this matter, SG-MT could seal the pores and defects of the PEO layer, but owing to the existence of some low cross-linking zones, the construction of the corrosion products could be expectable [85]. After 1 and 2 weeks of immersion, the majority of the linear rise in impedance as well as the more pronounced time constant at the lowest frequencies likely caused by the corrosion product construction [86]. Furthermore, R_{SG} and R_{mix} values of PSG were by far higher than PSG-MT in all immersion times, revealing its better corrosion protection

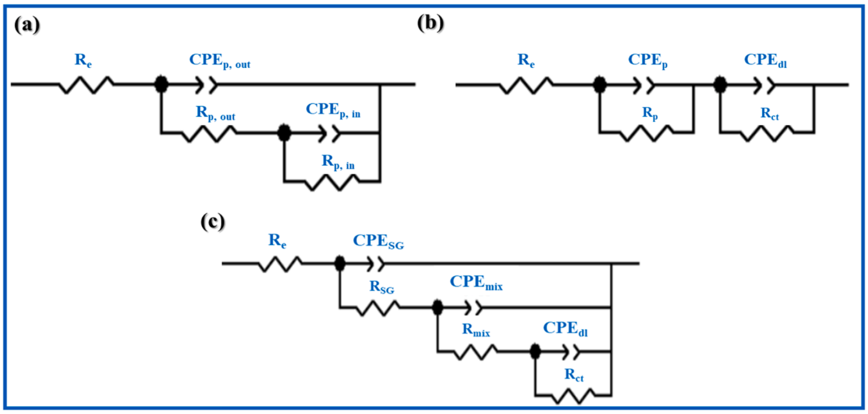

Fig. 9. Various types of the employed EECs to extract involved electrochemical parameters at different immersion times.

Table 2
The summarized outcome of the electrochemical parameters after fitting with some appropriate EECs.

Sample	*Immersion time in an hour (h) and week (w)*	R_{SG} (kΩ cm^2)	CPE_{SG} Y_0 (nΩ^{-1} cm^{-2} s ^{n})	*n*	R_{mix} or R_p (kΩ cm^2)	CPE_{mix} or CPE_p Y_0 (nΩ^{-1} cm^{-2} s ^{n})	*n*	R_{ct} (kΩ cm^2)	CPE_{dl} Y_0 (nΩ^{-1} cm^{-2} s ^{n})	*n*
PEO	6h	–	–	–	75	3593	0.79	293	16,051.00	0.96
	24h	–	–	–	36	72,787	0.64	20	8757.00	0.91
	48h	–	–	–	37	49,143	0.79	10	21,241.00	0.90
	72h	–	–	–	23	64,442	0.89	7	33,149.00	0.92
	1w	–	–	–	41	119,420	0.91	5	66,165.00	0.90
	2w	–	–	–	32	149,470	0.97	6	86,905.00	0.91
PSG	6h	679.29	2.18	0.96	36,584	31.16	0.44	153,600	2.90	0.82
	24h	312.65	2.43	0.96	2912	56.91	0.43	34,614	4.02	0.97
	48h	294.10	2.52	0.95	2313	51.11	0.44	45,228	9.33	0.94
	72h	276.12	2.53	0.96	4088	55.39	0.51	20,966	15.57	0.93
	1w	448.51	3.87	0.94	4412	22.75	0.74	25,744	198.94	0.52
	2w	59.61	5.04	0.92	4021	32.62	0.84	23,820	200.65	0.70
PSG-MT	6h	186.22	2.70	0.92	3682	25.16	0.60	381,000	41.01	0.72
	24h	134.82	3.13	0.92	2670	96.77	0.53	227,000	34.30	0.55
	48h	96.05	3.37	0.91	1066	165.79	0.52	13,167	109.14	0.78
	72h	60.58	3.36	0.92	379	286.50	0.48	27,109	75.76	0.67
	1w	62.51	5.57	0.88	610	415.87	0.49	52,410	400.25	0.81
	2w	33.64	9.97	0.87	328	532.35	0.60	63,849	585.68	0.70
PSG-AP	6h	77.60	22.72	0.84	12,765	113.42	0.68	12,972	14.74	0.90
	24h	3.41	104.82	0.77	1808	490.52	0.70	2275	4082.40	0.89
	48h	1.85	225.80	0.74	188	561.94	0.82	1110	1245.10	0.55
	72h	1.40	240.43	0.76	125	875.44	0.84	435	1933.90	0.61
	1w	–	–	–	104	13,400.00	0.72	6	7708.10	0.96
	2w	–	–	–	58	22,616.00	0.76	3	11,443.00	0.97
PSG-ZT	6h	2373.80	1.15	0.94	104,600	3.69	0.70	100,700	31.20	0.97
	24h	1918.50	1.19	0.94	91,703	3.71	0.70	184,600	28.47	0.93
	48h	1773.30	1.21	0.94	85,406	3.62	0.71	207,200	26.26	0.87
	72h	1568.80	1.23	0.94	77,906	3.61	0.71	223,200	25.97	0.82
	1w	1252.40	1.26	0.94	69,952	3.85	0.70	225,200	26.07	0.78
	2w	539.94	1.34	0.94	39,598	4.77	0.68	385,000	27.05	0.70

performance than PSG-MT.

By looking at PSG-AP spectra, a prompt drop-off of the protective properties (R_{SG} and R_{mix} values) was found so that almost no trace of the SG-AP could be observed after two weeks of exposure. Not only is the time constant depressed at higher frequencies but the low-frequency impedance is nearly the same with the unsealed PEO sample after two weeks of immersion test. This is also corroborated by the type of employed EEC for fitting, switched from three-time constants (Fig. 9c) up to 72 h exposure to two-time ones (Fig. 9b) which are the same utilized EEC for PEO at one and two weeks of dipping in the simulated corrosive solution. After one week of immersion, the duplex PEO/sol-gel coating was degraded, and the whole coating system including PEO and SG-AP layers exhibited only one time constant along with the frequency response of the substrate. Higher hydrophilicity, inadequate sealing properties, and insufficient barrier properties made the PSG-AP an unsatisfactory coating system in terms of protective features.

In contrast, PSG-ZT exhibited the highest protective functioning. Based on the Bode diagram, it had the highest coating capacitive behavior in the broad range of frequencies plus the time constant at high frequencies remained almost stable. The three-time constant EEC in Fig. 9c was employed to scrutinize the evolution of the electrochemical parameters during the immersion time. The R_{ct} values of PSG-ZT were the uttermost thanks to the development of reliable layer sealing, illustrating the most contribution in the complete system. The low-frequency impedance of the coated samples was compared upon immersion of up to two weeks in 0.1 M NaCl solution, as shown in Fig. 10.

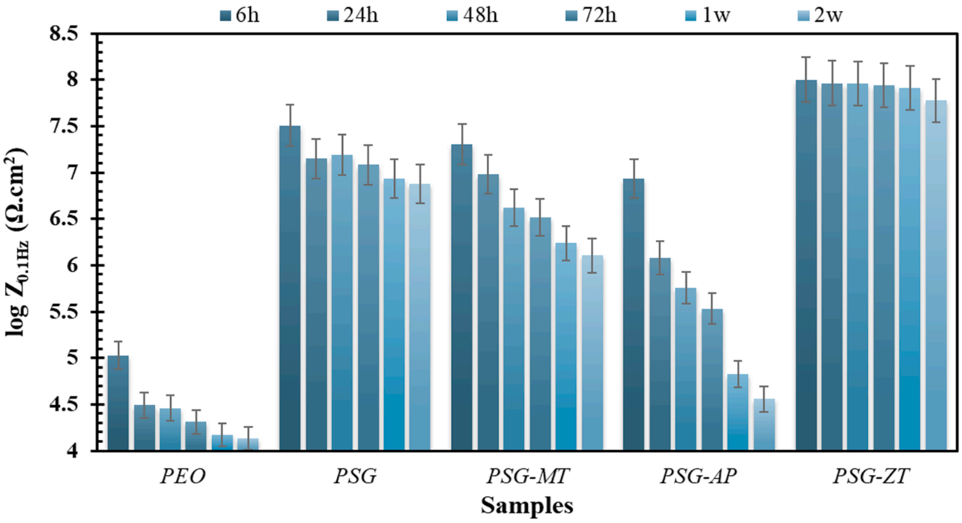

Fig. 10. Low-frequency impedance of the coated samples up to two weeks exposure to 0.1 M NaCl solution.

Fabrication of the sol-gel layer could enhance the protective properties of the distinct PEO layer thanks to their pore-filling properties, but their different chemical nature resulted in obtaining different protective performances. The decrement of the corrosion resistance properties of the PSG-MT is higher than PSG upon immersion. To enumerate, the modulus at 0.1 Hz of PSG-MT varied from $10^{7.31}$ to $10^{6.10}$ which was attested to by the EIS tests after 6 h and 2 w immersion times in the saline solution, respectively. Whereas the same EIS tests for PSG reported $10^{7.50}$ and $10^{6.85}$ in terms of low-frequency impedance. The cross-linking of the sol-gel network decreased in SG-MT as compared to the SG, which is why the lower corrosion resistance was attained in PSG-MT than PSG. The barrier properties of the PSG-ZT sample were almost unchanged, while the PSG-AP revealed a rapid deterioration in barrier properties. The reliable corrosion resistance properties of SG-ZT kept its features upon immersion in the aggressive solution, hindering the access of aggressive components to the substrate. It is worth noting that the creation of the cage-like structure of siloxane, as well as its hydrophobic properties, could play a crucial role in its inhibition performance. The considerable hydrophobic properties have been developed by the presence of significant organic parts in the composition.

To gain a brighter insight into the sealing ability of different sol-gel coatings, the effective capacitance of the mixed region (sol-gel plus PEO) and the R_{mix} (R_p in case of the unsealed PEO) are demonstrated in Fig. 11. The effective capacitance was calculated through below formula [87]:

$$C_{mix} = Y_{0,\ mix}^{1/n} R_{mix}^{(1-n)/n} \tag{3}$$

Capacitance is inversely proportional to the coating thickness (based on $C = \varepsilon\varepsilon_0 A/d$ formula). The thickness of the mixed region varies in the order of micrometers, hence relatively low values for the capacitance could be expected. Particularly in the case of PSG-ZT, there is also a uniform top layer over the PEO surface which enhances the thickness. Consequently, the lowest value of the effective capacitance for the PSG-ZT was anticipated. The relatively poor barrier properties of the unsealed PEO sample brought about a decrease in the R_p values after a short immersion time, followed by some ups and downs, which is mostly attributed to the corrosion product formation (Fig. 11a) [88]. The effective capacitance of this layer was drastically heightened because of the electrolyte ingress through the PEO coating (Fig. 11b). After the application of sol-gel coatings on the PEO layer, the R_{mix}, which shows the filled PEO pores with sol-gel sealing, increased, but with a drop in their protective performance as a function of immersion time, as exhibited in Fig. 11c_1 and Fig. 11c_2. The lowest and the highest values of R_{mix} in the PEO/sol-gel coating systems were attributed to the PSG-AP and PSG-ZT samples, respectively. The increment of the R_{mix} in the PSG sample after 72 h was probably because of the evolution of the

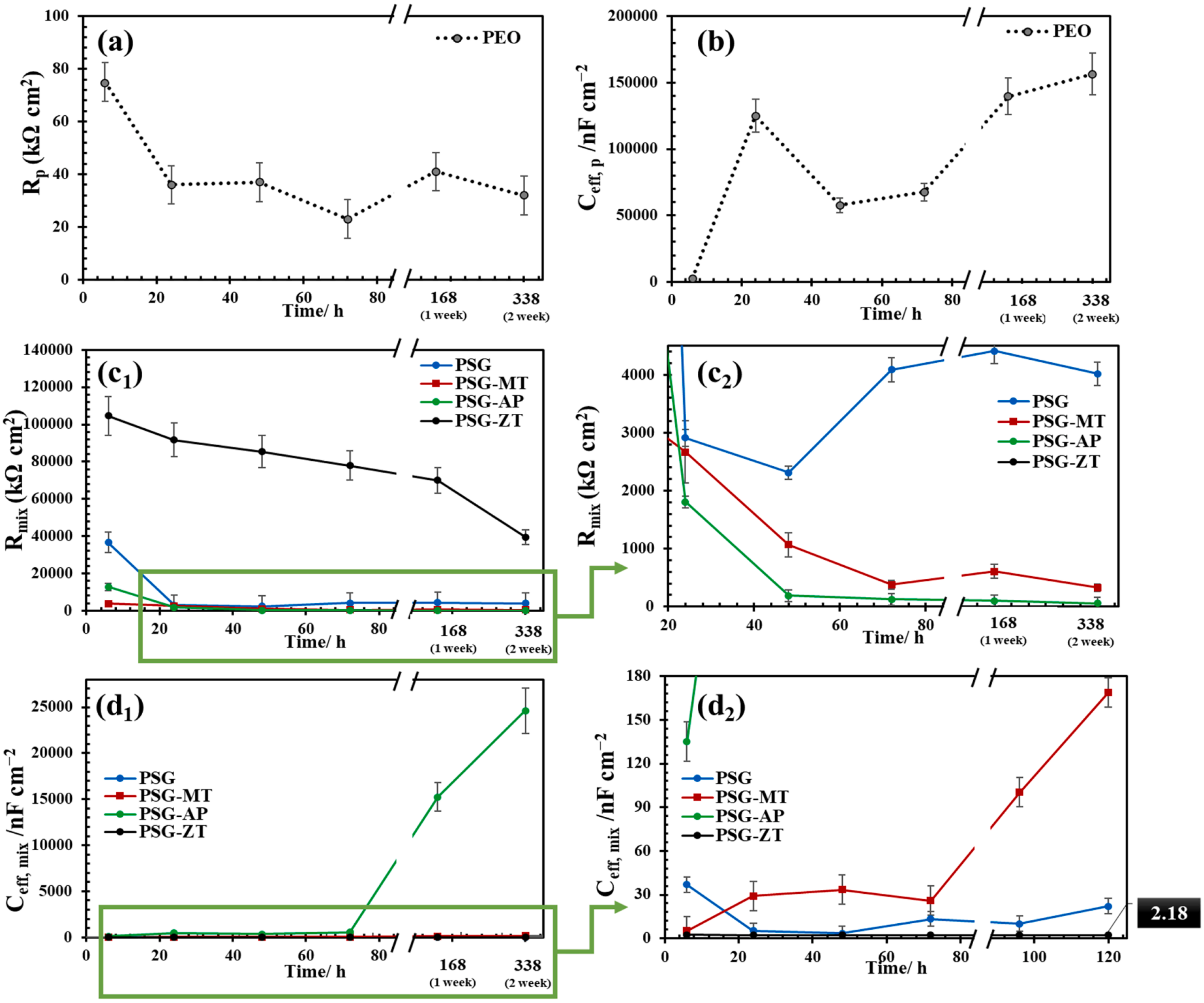

Fig. 11. The evolution of R_p (a) and $C_{eff,\ p}$ (b) for the PEO sample plus R_{mix} (c_1 and c_2) and $C_{eff,\ mix}$ (d_1 and d_2) for the duplex PEO/sol-gel coating system after two weeks immersion in 0.1 M NaCl solution.

hydrophilic corrosion products in this mixed region, which is in good agreement with another investigation [89]. By taking the C_{mix} versus time into account (Fig. 11d$_1$ and Fig. 11d$_2$), a huge diminishment was reported for all types of sol-gel/PEO coating systems as compared to the unsealed PEO. While coating permittivity is enhanced by water ingress through coatings, the coating capacitance is also increased [90,91]. For the PSG-AP, the C_{mix} enhanced significantly after 72 h, confirming the complete deterioration of the SG-AP coating on the PEO layer. In contrast to PSG-AP, the PSG-ZT showed an almost constant value for the C_{mix} during immersion, reaching 2.18 nF cm^{-2} at the end of the exposure. This originates from the fact that the SG-ZT not only had the highest coating thickness but could also penetrate through the pores, cracks, and other defects of the PEO layer. Therefore, the reliable barrier performance hinders the diffusion of the aggressive electrolyte, and

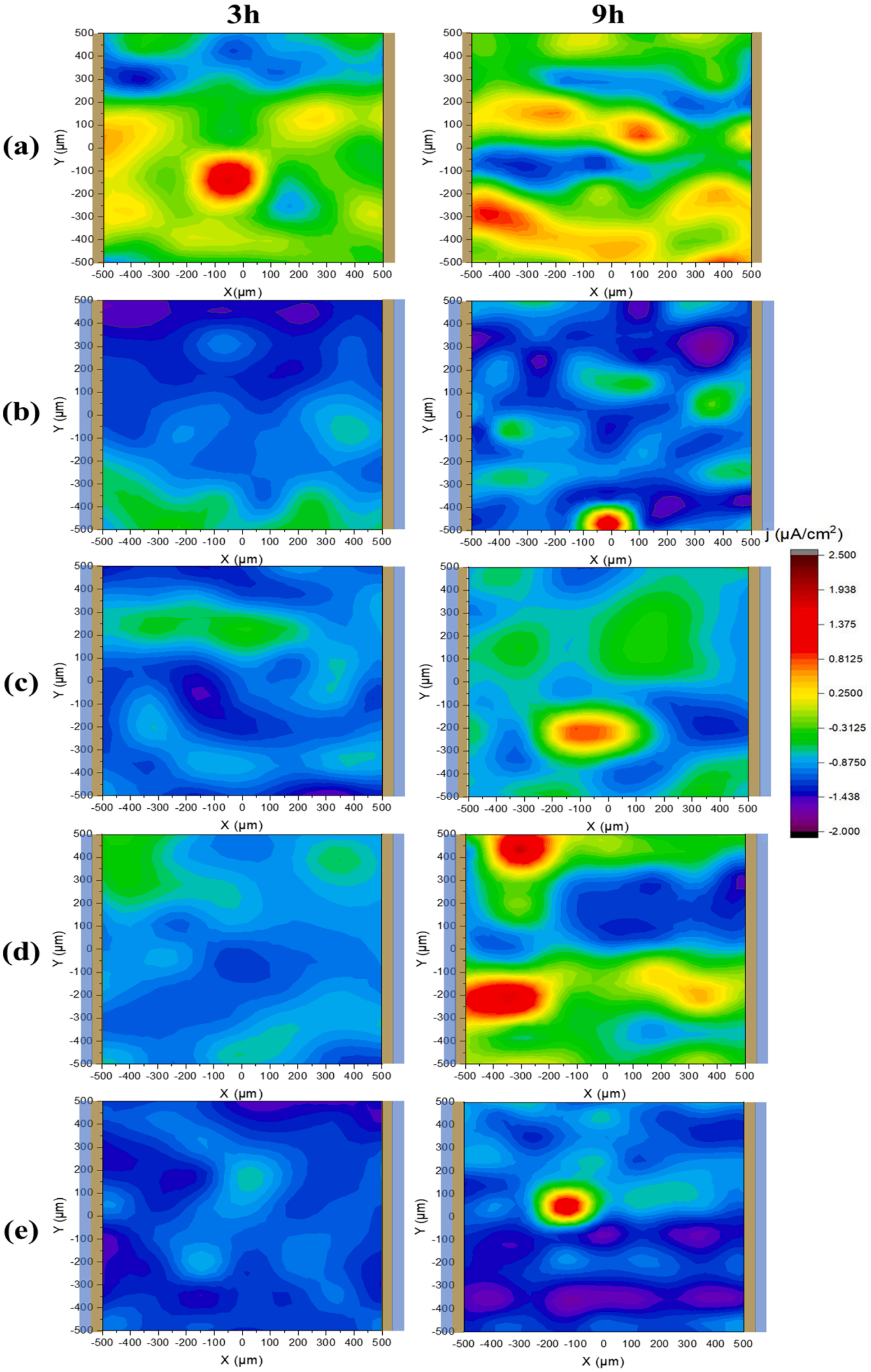

Fig. 12. SVET maps obtained from PEO (a), PSG (b), PSG-MT (c), PSG-AP (d), and PSG-ZT (e) samples after 3 and 9 h immersion in 15 mM NaCl solution. The PEO and sol-gel layers, respectively, are indicated by the brown and blue interfaces at the boundaries.

accordingly, the low amount of effective capacitance was recorded all over the immersion. All in all, the extent of the C_{mix} followed the order PEO>PSG-AP>PSG-MT>PSG>PSG-ZT. It is worthwhile mentioning that the associated capacitances (based on the CPE_{dl} values) are low due to the small exposed surface of the metallic interface but increase with immersion time mainly for PEO and PSG-AP, indicating an increase of the exposed surface for these two systems. Consequently, SG-ZT and SG-AP sol-gels were shown to be the superior and the inferior sealing sol-gels systems for the PEO layer on AA2024, respectively.

3.6. SVET analysis

To further scrutinize the role of different sealing sol-gel coatings on the corrosion resistance of the PEO layer, the SVET technique was employed in the 15 mM NaCl solution. The results attained from a cross-section of a coated sample embedded in a resin after 3 and 9 h of immersion are depicted in Fig. 12. In addition to the schematic representation of the experimental cell in Fig. 2, the PEO and sol-gel layers are denoted by the brown and blue interfaces at the boundaries in the SVET outcome, respectively. The cut-edge configuration might induce crevice corrosion so that the aggressive electrolyte could access the lateral parts of AA2024 via preferable pores, defects, and any other deficiencies, leading to the creation of a differential aeration cell [92]. On the other hand, AA2024 is susceptible to localized corrosion because of the low resistive properties of the passive layer on the S-phase, unmasking the substrate to an aggressive environment. While this happens, soluble Mg^{2+} leaches out from dissolving Mg into the solution, whose dynamics hinder the repassivation of an aluminum alloy at the S-phase sites [93]. The remnant copper forms a porous sponge structure with a high surface area that is primarily anodic, but it turns into cathodic sites for oxygen reduction after dealloying. In a neutral saline solution, the cathodic reaction is oxygen reduction according to the below [94]:

$$2H_2O + O_2 + 4e^- \rightarrow 4OH^- \tag{4}$$

The pH rises at Cu-rich remaining S-phase sites as they serve the cathode. The passive layer chemically dissolves as the pH reaches about 9 and bare aluminum will begin to selectively dissolve based on the below reaction [94]:

$$Al + 4OH^- \rightarrow Al(OH)_4^- + 3e^- \tag{5}$$

The local anodic activity somehow in the middle of the exposed area is likely related to the pitting corrosion of the substrate. The current density map for non-sealed PEO exhibited anodic activity at the PEO side, increasing from 3 to 9 h of exposure. The anodic attack linked to the porous PEO layer proceeded because of its coupling with the external alloy surface which is in direct contact with the electrolyte. Therefore, the rate of the corrosion reaction on the border regions is heightened from 3 to 9 h of the immersion test. By application of sol-gel coatings on the PEO layer, the intensity of anodic activity in the PEO region decreased at 3 h of exposure. The access of aggressive elements, such as water and Cl^- ion, to the substrate through the coating is by far facilitated in the cross-section mode as compared to the longitudinal configuration, which is why the decrement of protective functioning appeared after 9 h of exposure. Depression of anodic activity at the PEO borders was found in PSG, revealing the sealing of pores and other kinds of defects that induce a local type of corrosion. The performance of PSG-MT in the decrement of anodic current density at the PEO borders seemed to be less than PSG because of the sol-gel lower compactness. The intense anodic activity could not be observed preferentially at the PEO borders of PSG-MT, but still, PSG exhibited better sealing at the PEO borders. Insufficient sealing ability and poor protective performance of SG-AP resulted in the rapid deterioration of the coating at the borders. After 9 h of immersion, an intense local anodic activity was presented at the PEO border of PSG-AP, revealing the occurrence of possible classic crevice corrosion. In other words, the atrocious sealing ability of the SG-AP could also induce difficulty in water transport and make the water activity gradient. Surprisingly, the current density map of PSG-AP revealed that even if a coating is applied on the PEO layer, local corrosion is likely to happen if the sealing features do not play a role. Whereas in the PSG-ZT, as was shown in SEM images, its ability to not only seal the porosity but also form a top layer on the PEO coating provided the best protective performance, as demonstrated in the SVET result. Its sealing function was the most beneficial, illustrating no trace of anodic attack at the PEO borders in both reported SVET times of immersion.

4. Conclusion

The sealing ability of different sol-gel coatings for the PEO layer on AA2024 has been examined. The compactness, hydrophobicity, and impregnation features of the sol-gel layers play a significant role in terms of corrosion resistance properties. Considering this, the PSG-ZT had the best sealing ability thanks to the highest hydrophobicity, the construction of a homogenous layer over the PEO, as well as penetration through the intrinsic pores. As illustrated by SEM images, the sealing ability of PSG and PSG-MT was almost the same. However, the MTES precursor diminished the compactness of the coating because of the presence of one nonhydrolyzable methyl group in its molecular body, which is why PSG-MT showed lower corrosion protection performance than PSG. The poorest protective performance of the duplex PEO/sol-gel coating was related to the PSG-AP sample, owing to the relatively hydrophilic surface as well as the insufficient sealing ability for the PEO layer on AA2024. Finally, the evolution of the cage-like siloxane network, along with the ladder-like structure in the SG-ZT network development, could also enhance its barrier performance against aggressive elements.

CRediT authorship contribution statement

Sajjad Akbarzadeh: Investigation, Methodology, Validation, Writing – original draft. **Yoann Paint:** Investigation, Validation. **Marie-Georges Olivier:** Conceptualization, Methodology, Validation, Writing – review & editing, Supervision, Funding acquisition.

Declaration of Competing Interest

The authors declare that they have no known competing financial interests or personal relationships that could have appeared to influence the work reported in this paper.

Data availability

Data will be made available on request.

Acknowledgments

Authors gratefully acknowledge the financial support from the University of Mons (Action de Recherche Collective ARC SEALCERA).

Supplementary materials

Supplementary material associated with this article can be found, in the online version, at doi:10.1016/j.electacta.2023.141930.

References

[1] V. Jothi, A.Y. Adesina, A.M. Kumar, J.S.N. Ram, Influence of organic acids on the surface and corrosion resistant behavior of anodized films on AA2024 aerospace alloys in artificial seawater, Met. Mater. Int. 26 (2020) 1611–1620.
[2] X. Zhang, X. Zhou, T. Hashimoto, B. Liu, Localized corrosion in AA2024-T351 aluminium alloy: transition from intergranular corrosion to crystallographic pitting, Mater. Charact. 130 (2017) 230–236.

[3] N. Murer, R. Oltra, B. Vuillemin, O. Néel, Numerical modelling of the galvanic coupling in aluminium alloys: a discussion on the application of local probe techniques, Corros. Sci. 52 (2010) 130–139.

[4] M.B. Vukmirovic, N. Dimitrov, K. Sieradzki, Dealloying and corrosion of Al Alloy 2024-T3, J. Electrochem. Soc. 149 (2002) B428.

[5] K.A. Yasakau, J. Tedim, M.L. Zheludkevich, M.G.S. Ferreira, Smart self-healing coatings for corrosion protection of aluminium alloys, Handbook Smart Coatings Material Protection, Woodhead Publishing, Edited by Abdel Salam Hamdy Makhlouf (2014) 224–274.

[6] X. Verdalet-Guardiola, B. Fori, J.P. Bonino, S. Duluard, C. Blanc, Nucleation and growth mechanisms of trivalent chromium conversion coatings on 2024-T3 aluminium alloy, Corros. Sci. 155 (2019) 109–120.

[7] L. Hiltunen, H. Kattelus, M. Leskelä, M. Mäkelä, L. Niinistö, E. Nykänen, P. Soininen, M. Tiittad, Growth and characterization of aluminium oxide thin films deposited from various source materials by atomic layer epitaxy and chemical vapor deposition processes, Mater. Chem. Phys. 28 (1991) 379–388.

[8] G.M. Rao, A.V.G. Dilkush, Effect of physical vapour deposition coated and uncoated carbide tools in turning aluminium alloy-AA6063, Mater. Today Proc. 41 (2021) 1212–1219.

[9] S.A. Galedari, A. Mahdavi, F. Azarmi, Y. Huang, A. McDonald, A comprehensive review of corrosion resistance of thermally-sprayed and thermally-diffused protective coatings on steel structures, J. Therm. Spray Technol. 284 (28) (2019) 645–677.

[10] L.F. Wang, J. Sun, X.L. Yu, Y. Shi, X.G. Zhu, L.Y. Cheng, H.H. Liang, B. Yan, L. J. Guo, Enhancement in mechanical properties of selectively laser-melted AlSi10Mg aluminum alloys by T6-like heat treatment, Mater. Sci. Eng. A. 734 (2018) 299–310.

[11] A.I. Ryabchikov, E.B. Kashkarov, A.E. Shevelev, A. Obrosov, D.O. Sivin, Surface modification of Al by high-intensity low-energy Ti-ion implantation: microstructure, mechanical and tribological properties, Surf. Coat. Technol. 372 (2019) 1–8.

[12] V.R. Capelossi, M. Poelman, I. Recloux, R.P.B. Hernandez, H.G. De Melo, M. G. Olivier, Corrosion protection of clad 2024 aluminum alloy anodized in tartaric-sulfuric acid bath and protected with hybrid sol–gel coating, Electrochim. Acta. 124 (2014) 69–79.

[13] G.A. Mengesha, J.P. Chu, B.S. Lou, J.W. Lee, Effects of processing parameters on the corrosion performance of plasma electrolytic oxidation grown oxide on commercially pure aluminum, Metals 10 (2020) 394 (Basel).

[14] R. del Olmo, M. Mohedano, P. Visser, E. Matykina, R. Arrabal, Flash-PEO coatings loaded with corrosion inhibitors on AA2024, Surf. Coat. Technol. 402 (2020), 126317.

[15] R. Arrabal, M. Mohedano, E. Matykina, A. Pardo, B. Mingo, M.C. Merino, Characterization and wear behaviour of PEO coatings on 6082-T6 aluminium alloy with incorporated α-Al_2O_3 particles, Surf. Coat. Technol. 269 (2015) 64–73.

[16] D.V. Mashtalyar, K.V. Nadaraia, A.S. Gnedenkov, I.M. Imshinetskiy, M.A. Piatkova, A.I. Pleshkova, E.A. Belov, V.S. Filonina, S.N. Suchkov, S.L. Sinebryukhov, S. V. Gnedenkov, Bioactive coatings formed on titanium by plasma electrolytic oxidation: composition and properties, Materials 13 (2020) 4121 (Basel).

[17] P. Molaeipour, S.R. Allahkaram, S. Akbarzadeh, Corrosion inhibition of Ti6Al4V alloy by a protective plasma electrolytic oxidation coating modified with boron carbide nanoparticles, Surf. Coat. Technol. 430 (2022), 127987.

[18] B. Hamrahi, B. Yarmand, A. Massoudi, Improved in-vitro corrosion performance of titanium using a duplex system of plasma electrolytic oxidation and graphene oxide incorporated silane coatings, Surf. Coat. Technol. 422 (2021), 127558.

[19] B. Mingo, Y. Guo, A. Němcová, A. Gholinia, M. Mohedano, M. Sun, A. Matthews, A. Yerokhin, Incorporation of halloysite nanotubes into forsterite surface layer during plasma electrolytic oxidation of AM50 Mg alloy, Electrochim. Acta 299 (2019) 772–788.

[20] G. Peitao, T. Mingyang, Z. Chaoyang, Tribological and corrosion resistance properties of graphite composite coating on AZ31 Mg alloy surface produced by plasma electrolytic oxidation, Surf. Coat. Technol. 359 (2019) 197–205.

[21] K. Li, W. Li, G. Zhang, W. Zhu, F. Zheng, D. Zhang, M. Wang, Effects of Si phase refinement on the plasma electrolytic oxidation of eutectic Al-Si alloy, J. Alloy. Compd. 790 (2019) 650–656.

[22] H.J. Xie, Y.L. Cheng, S.X. Li, J.H. Cao, L. Cao, Wear and corrosion resistant coatings on surface of cast A356 aluminum alloy by plasma electrolytic oxidation in moderately concentrated aluminate electrolytes, Trans. Nonferrous Met. Soc. China. 27 (2017) 336–351.

[23] L. Wang, L. Chen, Z. Yan, W. Fu, Optical emission spectroscopy studies of discharge mechanism and plasma characteristics during plasma electrolytic oxidation of magnesium in different electrolytes, Surf. Coat. Technol. 205 (2010) 1651–1658.

[24] L.O. Snizhko, A.L. Yerokhin, A. Pilkington, N.L. Gurevina, D.O. Misnyankin, A. Leyland, A. Matthews, Anodic processes in plasma electrolytic oxidation of aluminium in alkaline solutions, Electrochim. Acta. 49 (2004) 2085–2095.

[25] M. Mohedano, X. Lu, E. Matykina, C. Blawert, R. Arrabal, M.L. Zheludkevich, Plasma electrolytic oxidation (PEO) of metals and alloys, Encycl. Interfacial Chem. Surf. Sci. Electrochem. (2018) 423–438.

[26] M. Treviño, R.D. Mercado-Solis, R. Colás, A. Pérez, J. Talamantes, A. Velasco, Erosive wear of plasma electrolytic oxidation layers on aluminium alloy 6061, Wear 301 (2013) 434–441.

[27] L. Pezzato, R. Babbolin, P. Cerchier, M. Marigo, P. Dolcet, M. Dabalà, K. Brunelli, Sealing of PEO coated AZ91magnesium alloy using solutions containing neodymium, Corros. Sci. 173 (2020), 108741.

[28] D.V. Mashtalyar, K.V. Nadaraia, I.M. Imshinetskiy, E.A. Belov, V.S. Filonina, S. N. Suchkov, S.L. Sinebryukhov, S.V. Gnedenkov, Composite coatings formed on Ti by PEO and fluoropolymer treatment, Appl. Surf. Sci 536 (2021), 147976.

[29] J. Joo, D. Kim, H.S. Moon, K. Kim, J. Lee, Durable anti-corrosive oil-impregnated porous surface of magnesium alloy by plasma electrolytic oxidation with hydrothermal treatment, Appl. Surf. Sci. 509 (2020), 145361.

[30] L. Pezzato, K. Brunelli, R. Babbolin, P. Dolcet, M. Dabalà, Sealing of PEO coated AZ91 magnesium alloy using la-based solutions, Int. J. Corros. (2017), 2017.

[31] S. Akbarzadeh, M. Ramezanzadeh, B. Ramezanzadeh, M. Mahdavian, R. Naderi, Fabrication of highly effective polyaniline grafted carbon nanotubes to induce active protective functioning in a silane coating, Ind. Eng. Chem. Res. 58 (2019) 20309–20322.

[32] A. Mehner, H.W. Zoch, W. Datchary, G. Pongs, Sol-gel coatings for high precision optical molds, CIRP Ann. 55 (2006) 589–592.

[33] J.D. Mackenzie, E.P. Bescher, Physical properties of sol-gel coatings, J. Sol Gel Sci. Technol. 191 (19) (2000) 23–29.

[34] S. Akbarzadeh, K. Akbarzadeh, M. Ramezanzadeh, R. Naderi, M. Mahdavian, M. G. Olivier, Corrosion resistance enhancement of a sol-gel coating by incorporation of modified carbon nanotubes: artificial neural network (ANN) modeling and experimental explorations, Prog. Org. Coat. 174 (2023), 107296.

[35] D. Balgude, A. Sabnis, Sol-gel derived hybrid coatings as an environment friendly surface treatment for corrosion protection of metals and their alloys, J. Sol Gel Sci. Technol. 64 (2012) 124–134.

[36] W.J. van Ooij, D. Zhu, M. Stacy, A. Seth, T. Mugada, J. Gandhi, P. Puomi, Corrosion protection properties of organofunctional silanes—an overview, Tsinghua Sci. Technol. 10 (2005) 639–664.

[37] D. Wang, G.P. Bierwagen, Sol-gel coatings on metals for corrosion protection, Prog. Org. Coat. 64 (2009) 327–338.

[38] M. Oubaha, P. Etienne, S. Calas, R. Sempere, J.M. Nedelec, Y. Moreau, Spectroscopic characterization of sol–gel organo-siloxane materials synthesized from aliphatic and aromatic alcoxysilanes, J. Non Cryst. Solids 351 (2005) 2122–2128.

[39] P.C.R. Varma, J. Colreavy, J. Cassidy, M. Oubaha, B. Duffy, C. McDonagh, Effect of organic chelates on the performance of hybrid sol–gel coated AA 2024-T3 aluminium alloys, Prog. Org. Coat. 66 (2009) 406–411.

[40] G.I. Spijksma, H.J.M. Bouwmeester, D.H.A. Blank, V.G. Kessler, Stabilization and destabilization of zirconium propoxide precursors by acetylacetone, Chem. Commun. (2004) 1874–1875.

[41] F. Girardi, F. Graziola, P. Aldighieri, L. Fedrizzi, S. Gross, R. Di Maggio, Inorganic–organic hybrid materials with zirconium oxoclusters as protective coatings on aluminium alloys, Prog. Org. Coat. 62 (2008) 376–381.

[42] E. Merino, A. Durán, Y. Castro, Integrated corrosion-resistant system for AZ31B Mg alloy via plasma electrolytic oxidation (PEO) and sol-gel processes, Int. J. Appl. Glas. Sci. 12 (2021) 519–530.

[43] L. Pezzato, M. Rigon, A. Martucci, K. Brunelli, M. Dabalà, Plasma electrolytic oxidation (PEO) as pre-treatment for sol-gel coating on aluminum and magnesium alloys, Surf. Coat. Technol. 366 (2019) 114–123.

[44] M. Toorani, M. Aliofkhazraei, M. Mahdavian, R. Naderi, Effective PEO/silane pretreatment of epoxy coating applied on AZ31B Mg alloy for corrosion protection, Corros. Sci. 169 (2020), 108608.

[45] P. Fernández-López, S.A. Alves, I. Azpitarte, J.T. San-José, R. Bayón, Corrosion and tribocorrosion protection of novel PEO coatings on a secondary cast Al-Si alloy: influence of polishing and sol-gel sealing, Corros. Sci. 207 (2022), 110548.

[46] S. Akbarzadeh, L.S. Santos, V. Vitry, Y. Paint, M.G. Olivier, Improvement of the corrosion performance of AA2024 alloy by a duplex PEO/clay modified sol-gel nanocomposite coating, Surf. Coat. Technol. 434 (2022), 128168.

[47] L. Sopchenski, J. Robert, M. Touzin, A. Tricoteaux, M.G. Olivier, Improvement of wear and corrosion protection of PEO on AA2024 via sol-gel sealing, Surf. Coat. Technol. 417 (2021), 127195.

[48] V. Ntomprougkidis, J. Martin, A. Nominé, G. Henrion, Sequential run of the PEO process with various pulsed bipolar current waveforms, Surf. Coat. Technol. 374 (2019) 713–724.

[49] V. Dehnavi, B.L. Luan, D.W. Shoesmith, X.Y. Liu, S. Rohani, Effect of duty cycle and applied current frequency on plasma electrolytic oxidation (PEO) coating growth behavior, Surf. Coat. Technol. 226 (2013) 100–107.

[50] H. Costenaro, A. Lanzutti, Y. Paint, L. Fedrizzi, M. Terada, H.G. de Melo, M. G. Olivier, Corrosion resistance of 2524 Al alloy anodized in tartaric-sulphuric acid at different voltages and protected with a TEOS-GPTMS hybrid sol-gel coating, Surf. Coat. Technol. 324 (2017) 438–450.

[51] M. Toorani, M. Aliofkhazraei, M. Mahdavian, R. Naderi, Superior corrosion protection and adhesion strength of epoxy coating applied on AZ31 magnesium alloy pre-treated by PEO/Silane with inorganic and organic corrosion inhibitors, Corros. Sci. 178 (2021), 109065.

[52] P. Rodič, J. Iskra, I. Milošev, A hybrid organic-inorganic sol-gel coating for protecting aluminium alloy 7075-T6 against corrosion in Harrison᾽s solution, J. Sol Gel Sci. Technol. 70 (2014) 90–103.

[53] N.C. Rosero-Navarro, S.A. Pellice, Y. Castro, M. Aparicio, A. Durán, Improved corrosion resistance of AA2024 alloys through hybrid organic–inorganic sol–gel coatings produced from sols with controlled polymerisation, Surf. Coat. Technol. 203 (2009) 1897–1903.

[54] K. Studer, C. Decker, E. Beck, R. Schwalm, Overcoming oxygen inhibition in UV-curing of acrylate coatings by carbon dioxide inerting, Part I, Prog. Org. Coat. 48 (2003) 92–100.

[55] B. Ramezanzadeh, Z. Haeri, M. Ramezanzadeh, A facile route of making silica nanoparticles-covered graphene oxide nanohybrids (SiO_2-GO); fabrication of SiO_2-GO/epoxy composite coating with superior barrier and corrosion protection performance, Chem. Eng. J. 303 (2016) 511–528.

[56] F. Deflorian, S. Rossi, L. Fedrizzi, M. Fedel, Integrated electrochemical approach for the investigation of silane pre-treatments for painting copper, Prog. Org. Coat. 63 (2008) 338–344.
[57] P. Molaeipour, M. Ramezanzadeh, B. Ramezanzadeh, Stachys byzantina extract: a green biocompatible molecules source for graphene skeletons generation on the carbon steel for superior corrosion mitigation, Bioelectrochemistry 143 (2022), 107970.
[58] A.L. Smith, Infrared spectra-structure correlations for organosilicon compounds, Spectrochim. Acta 16 (1960) 87–105.
[59] G. Tan, L. Zhang, C. Ning, X. Liu, J. Liao, Preparation and characterization of APTES films on modification titanium by SAMs, Thin Solid Films 519 (2011) 4997–5001.
[60] N. Majoul, S. Aouida, B. Bessaïs, Progress of porous silicon APTES-functionalization by FTIR investigations, Appl. Surf. Sci. 331 (2015) 388–391.
[61] J. Wen, G.L. Wilkes, Organic/inorganic hybrid network materials by the sol-gel approach, Chem. Mater. 8 (1996) 1667–1681.
[62] V. Tagliazucca, E. Callone, S. Dirè, Influence of synthesis conditions on the cross-link architecture of silsesquioxanes prepared by in situ water production route, J. Sol Gel Sci. Technol. 60 (2011) 236–245.
[63] R. Samiee, B. Ramezanzadeh, M. Mahdavian, E. Alibakhshi, Corrosion inhibition performance and healing ability of a hybrid silane coating in the presence of praseodymium (III) cations, J. Electrochem. Soc. 165 (2018) C777–C786.
[64] A. Shimojima, K. Kuroda, Alkoxy- and silanol-functionalized cage-type oligosiloxanes as molecular building blocks to construct nanoporous materials, Molecules 25 (2020) 524, 25 (2020) 524.
[65] M. Fedel, E. Callone, M. Fabbian, F. Deflorian, S. Dirè, Influence of Ce3+ doping on molecular organization of Si-based organic/inorganic sol-gel layers for corrosion protection, Appl. Surf. Sci. 414 (2017) 82–91.
[66] P. Rodič, J. Iskra, I. Milošev, Study of a sol–gel process in the preparation of hybrid coatings for corrosion protection using FTIR and 1H NMR methods, J. Non. Cryst. Solids. 396–397 (2014) 25–35.
[67] I. Milošev, B. Kapun, P. Rodič, J. Iskra, Hybrid sol–gel coating agents based on zirconium(IV) propoxide and epoxysilane, J. Sol Gel Sci. Technol. 74 (2015) 447–459.
[68] N. Mileti, L.T.T. Fahriansyah, K. Nguyen, Loos, Formation, topography and reactivity of Candida antarctica lipase B immobilized on silicon surface, Biocatal. Biotransform. 28 (2010) 357–369.
[69] J.O. Otalvaro, M. Avena, M. Brigante, Adsorption of organic pollutants by amine functionalized mesoporous silica in aqueous solution. Effects of pH, ionic strength and some consequences of APTES stability, J. Environ. Chem. Eng. 7 (2019), 103325.
[70] P. Innocenzi, T. Kidchob, T. Yoko, Hybrid organic-inorganic sol-gel materials based on epoxy-amine systems, J. Sol Gel Sci. Technol. 353 (35) (2005) 225–235.
[71] R.S. Sonawane, S.G. Hegde, M.K. Dongare, Preparation of titanium(IV) oxide thin film photocatalyst by sol–gel dip coating, Mater. Chem. Phys. 77 (2003) 744–750.
[72] M.V. Reyes-Peces, A. Pérez-Moreno, D.M. De-Los-santos, M.D.M. Mesa-Díaz, G. Pinaglia-Tobaruela, J.I. Vilches-Pérez, R. Fernández-Montesinos, M. Salido, N. de la Rosa-Fox, M. Piñero, Chitosan-GPTMS-silica hybrid mesoporous aerogels for bone tissue engineering, Polymers 12 (2020) 2723 (Basel).
[73] G. Rosace, E. Guido, C. Colleoni, G. Barigozzi, Influence of textile structure and silica based finishing on thermal insulation properties of cotton fabrics, Int. J. Polym. Sci. 2016 (2016).
[74] I.A. Ciobotaru, I. Maior, D.I. Vaireanu, A. Cojocaru, S. Caprarescu, I.E. Ciobotaru, The determination of the optimum hydrolysis time for silane films deposition, Appl. Surf. Sci. 371 (2016) 275–280.
[75] D.Y. Nadargi, S.S. Latthe, H. Hirashima, A.V. Rao, Studies on rheological properties of methyltriethoxysilane (MTES) based flexible superhydrophobic silica aerogels, Microporous Mesoporous Mater. 117 (2009) 617–626.
[76] S. Cui, Y. Liu, M.H. Fan, A.T. Cooper, B.L. Lin, X.Y. Liu, G.F. Han, X.D. Shen, Temperature dependent microstructure of MTES modified hydrophobic silica aerogels, Mater. Lett. 65 (2011) 606–609.
[77] J. Kim, P. Seidler, L.S. Wan, C. Fill, Formation, structure, and reactivity of amino-terminated organic films on silicon substrates, J. Colloid Interface Sci. 329 (2009) 114–119.
[78] C.L. Alexander, B. Tribollet, M.E. Orazem, Contribution of surface distributions to constant-phase-element (CPE) behavior: 1. Influence of roughness, Electrochim. Acta. 173 (2015) 416–424.
[79] W. Liu, Y. Pu, H. Liao, Y. Lin, W. He, Corrosion and wear behavior of PEO coatings on D16T aluminum alloy with different concentrations of graphene, Coatings 10 (2020) 249, 10 (2020) 249.
[80] M. Zhu, Y. Song, K. Dong, D. Shan, E.H. Han, Correlation between the transient variation in positive/negative pulse voltages and the growth of PEO coating on 7075 aluminum alloy, Electrochim. Acta 411 (2022), 140056.
[81] S. Amand, M. Musiani, M.E. Orazem, N. Pébère, B. Tribollet, V. Vivier, Constant-phase-element behavior caused by inhomogeneous water uptake in anti-corrosion coatings, Electrochim. Acta 87 (2013) 693–700.
[82] H.H. Hernández, A.M.R. Reynoso, J.C.T. González, C.O.G. Morán, J.G. M. Hernández, A.M. Ruiz, J.M. Hernández, R.O. Cruz, Electrochemical impedance spectroscopy (EIS): a review study of basic aspects of the corrosion mechanism applied to steels, Electrochem. Impedance Spectrosc. (2020).
[83] F. Yang, T. Liu, J. Li, S. Qiu, H. Zhao, Anticorrosive behavior of a zinc-rich epoxy coating containing sulfonated polyaniline in 3.5% NaCl solution, RSC Adv. 8 (2018) 13237–13247.
[84] M. Mo, W. Zhao, Z. Chen, E. Liu, Q. Xue, Corrosion inhibition of functional graphene reinforced polyurethane nanocomposite coatings with regular textures, RSC Adv. 6 (2016) 7780–7790.
[85] M. Ramezanzadeh, B. Ramezanzadeh, M. Mahdavian, G. Bahlakeh, Development of metal-organic framework (MOF) decorated graphene oxide nanoplatforms for anti-corrosion epoxy coatings, Carbon N. Y. 161 (2020) 231–251.
[86] R. Farrakhov, O. Melnichuk, E. Parfenov, V. Mukaeva, A. Raab, V. Sheremetyev, Y. Zhukova, S. Prokoshkin, Comparison of biocompatible coatings produced by plasma electrolytic oxidation on cp-Ti and Ti-Zr-Nb superelastic alloy, Coatings 11 (2021) 401.
[87] B. Hirschorn, M.E. Orazem, B. Tribollet, V. Vivier, I. Frateur, M. Musiani, Determination of effective capacitance and film thickness from constant-phase-element parameters, Electrochim. Acta 55 (2010) 6218–6227.
[88] S. Akbarzadeh, M. Ramezanzadeh, B. Ramezanzadeh, G. Bahlakeh, A green assisted route for the fabrication of a high-efficiency self-healing anti-corrosion coating through graphene oxide nanoplatform reduction by Tamarindus indiaca extract, J. Hazard. Mater. 390 (2020), 122147.
[89] C.N. Njoku, W. Bai, I.O. Arukalam, L. Yang, B. Hou, D.I. Njoku, Y. Li, Epoxy-based smart coating with self-repairing polyurea-formaldehyde microcapsules for anticorrosion protection of aluminum alloy AA2024, J. Coat. Technol. Res. 17 (2020) 797–813.
[90] K. Ogle, S. Morel, N. Meddahi, An electrochemical study of the delamination of polymer coatings on galvanized steel, Corros. Sci. 47 (2005) 2034–2052.
[91] S. Akbarzadeh, R. Naderi, M. Mahdavian, Fabrication of a highly protective silane composite coating with limited water uptake utilizing functionalized carbon nanotubes, Compos. Part B Eng. 175 (2019), 107109.
[92] L. Pezzato, L.B. Coelho, R. Bertolini, A.G. Settimi, K. Brunelli, M. Olivier, M. Dabalà, Corrosion and mechanical properties of plasma electrolytic oxidation-coated AZ80 magnesium alloy, Mater. Corros. 70 (2019) 2103–2112.
[93] N. Dimitrov, J.A. Mann, M. Vukmirovic, K. Sieradzki, Dealloying of Al2CuMg in alkaline media, J. Electrochem. Soc. 147 (2000) 3283.
[94] J.O. Park, C.H. Paik, Y.H. Huang, R.C. Alkire, Influence of Fe-rich intermetallic inclusions on pit initiation on aluminum alloys in aerated NaCl, J. Electrochem. Soc. 146 (1999) 517–523.